

1 Remote and in situ observations of an unusual
2 Earth-directed Coronal Mass Ejection from multiple
3 viewpoints

T. Nieves-Chinchilla¹, R. Colaninno², A. Vourlidas², A. Szabo³,
R.P.Lepping³, S.A.Boardsen⁴, B.J. Anderson⁵, and H. Korth⁵

T. Nieves-Chinchilla, CUA, Teresa.Nieves@nasa.gov

¹ Catholic University of America,
Washington, DC, USA.

² Space Sciences Division, Naval Research
Laboratory, Washington, DC, USA.

³ Heliospheric Physic Laboratory, NASA
Goddard Space Flight Center, Greenbelt,
USA

⁴ Heliophysics Science Division, NASA
Goddard Space Flight Center, Greenbelt,
USA

⁵ The Johns Hopkins University Applied
Physics Laboratory, Laurel, MD, USA.

Abstract.

During June 16-21, 2010, an Earth-directed Coronal Mass Ejection (CME) event was observed by instruments onboard STEREO, SOHO, MESSENGER and Wind. This event was the first direct detection of a rotating CME in the middle and outer corona. Here, we carry out a comprehensive analysis of the evolution of the CME in the interplanetary medium comparing in-situ and remote observations, with analytical models and three-dimensional reconstructions. In particular, we investigate the parallel and perpendicular cross section expansion of the CME from the corona through the heliosphere up to 1 AU. We use height-time measurements and the Gradual Cylindrical Shell (GCS) technique to model the imaging observations, remove the projection effects, and derive the 3-dimensional extent of the event. Then, we compare the results with in-situ analytical Magnetic Cloud (MC) models, and with geometrical predictions from past works. We find that the parallel (along the propagation plane) cross section expansion agrees well with the in-situ model and with the Bothmer & Schwenn [1998] empirical relationship based on in-situ observations between 0.3 and 1 AU. Our results effectively extend this empirical relationship to about 5 solar radii. The expansion of the perpendicular diameter agrees very well with the in-situ results at MESSENGER (~ 0.5 AU) but not at 1 AU. We also find a slightly different, from Bothmer & Schwenn [1998], empirical relationship for the perpendicular expansion. More importantly, we find no evidence that the CME undergoes a significant latitudinal over-expansion as it is commonly assumed.

27 Instead, we find evidence that effects due to CME rotation and expansion
28 can be easily confused in the images leading to a severe overestimation of
29 the proper 3D size of the event. Finally, we find that the reconstructions of
30 the CME morphology from the in-situ observations at 1 AU are in agreement
31 with the remote sensing observations but they show a big discrepancy at MES-
32 SINGER. We attribute this discrepancy to the ambiguity of selecting the
33 proper boundaries due to the lack of accompanying plasma measurements.

1. Introduction

34 The heliospheric counterparts of Coronal Mass Ejections (CMEs), usually studied with
35 in-situ instrumentation, are referred as Interplanetary CMEs (ICMEs). The study of the
36 initiation, propagation and evolution of ICMEs is of special interest, since they are the
37 primary cause of geo-effective space weather events. Knowledge of the magnetic structure
38 of CMEs in the interplanetary medium is crucial to connect the CME origins on the Sun
39 to their effects on the Earth [Hidalgo et al., 2011].

40 In-situ measurements suggest that a third of ICMEs observed have a magnetic flux
41 rope structure known as a Magnetic Cloud (MC) [Gosling et al., 1990]. The in-situ
42 features of MCs include an elevation in the magnetic field magnitude, rotation in at least
43 one component of the magnetic field, and low proton- β plasma parameter [Burlaga et
44 al., 1981]. Naturally, ICME studies are usually focused on those events that contain
45 MCs. There are two main reasons: one, because of their relatively well-defined magnetic
46 topology, and, two, because MCs drive the biggest geomagnetic storms (e.g., Richardson
47 et al. [2002]).

48 Many of the models developed for MCs are based on the concept of a flux-rope in a
49 force-free configuration (Burlaga [1988], Lepping et al. [1990]). These models take into
50 consideration only a subset of the characteristics of MCs as defined by Burlaga et al.
51 [1981]. Other models relax the force-free condition [Owens, 2006] and attempt to describe
52 MCs in their full context with a minimum set of assumptions. Or instead, models as
53 that of Hidalgo & Nieves-Chinchilla [2012] represent an analytical approach to the global
54 magnetic field topology of MCs focussing in the understanding of the physical mechanism

inside the whole structure. However, it is fair to say that they all describe a limited subset of the properties of MCs.

A relatively recent technique, based on solving the Grad-Shafranov equation inside MCs [Hu & Sonnerup, 2002] enables to reconstruct the MC cross section, under a different set of assumptions, and provides a new understanding of these interplanetary events. Such results show that MCs are far from being circular [Möstl et al., 2008].

In all cases, the modeling of in-situ observations of MCs is based on a one-dimensional set of measurements made only along a line cutting through the structure. These measurements are clearly insufficient to describe the evolution of the structure since ICMEs may undergo significant changes from the inner corona and, even, during they pass over an observing spacecraft.

Using Helios data, Bothmer & Schwenn [1998] carried out a MC survey at different solar distances (from 0.3 AU to 1 AU). Assuming a circular cross-section, they derived the rate of expansion for the cross-section

$$Diameter = a(x)^n \quad \text{with} \quad n = 0.78 \quad (1)$$

where x is the heliocentric distance, and a is a constant. This rate of cross-section expansion implies that the density decreases proportionally as $x^{-2.4}$ which in turn implies that plasma pressure is more important in the initial stages of the ICME than at 1 AU, and should be taken into account in the ICME expansion.

Magnetohydrodynamic (MHD) 3D simulations predict a distortion of the MC cross-section, known as 'pancaking', with the thinning taking place in the propagation direction [Riley & Crooker, 2004; Riley et al., 2004]. This distortion is sometimes observed in the remote sensing data for ideal CME-spacecraft configuration.

78 From the point of view of the in-situ observations, an asymmetric profile in the magnetic
79 field magnitude is thought to be a consequence of this flattening of the ICME. On the
80 other hand, an asymmetric magnetic field profile accompanied with a linearly decreasing
81 velocity is indicative of overall cross-section expansion. Both, the concepts of expansion
82 and distortion, are closely related to the focus of this work.

83 The in-situ analysis can now be tested using remote sensing observations from the
84 SECCHI imagers [Howard et al., 2008] aboard the STEREO mission [Kaiser et al., 2008],
85 which image the ICMEs at the same locations as the in-situ observations in the heliosphere.
86 On the solar side, the SDO mission provides high-resolution observations of the solar
87 corona and the photosphere for the understanding of solar dynamics. The EUV disk
88 imagers and white light coronagraphs on STEREO can currently provide side views of
89 the CME initiation and follow the CME all the way to 1 AU and beyond.

90 Forward modeling concepts, such as that of Thernisien et al. [2006]; Thernisien [2011],
91 can be used to fit the CME flux rope in imaging observations from multiple vantage
92 points and provide geometrical information, such as orientation, propagation direction
93 and 3D structure. The model results become increasingly more robust when observations
94 from different viewpoints are used. The analysis uses images from the coronagraphs on
95 STEREO and SOHO. For simplicity and to keep the number of free parameters to a
96 minimum, this model assumes that the flux-rope has a circular cross-section. However,
97 this may not always be correct for the propagation of CMEs in the interplanetary medium.

98 Recently, Savani et al. [2011] derived a geometrical semi-empirical aspect ratio (χ) for
99 the CME's cross-section (i.e. relationship between major and minor radius) given by the

100 expression,

$$101 \quad \chi = \frac{R(r_0/L_0)}{r_0 + A(R - L_0)} \quad (2)$$

102 where R is distance from the Sun, r_0 is the initial circular radius ($\sim 1R_S$), L_0 is the initial
 103 distance from the Sun ($\sim 2R_S$), and A is the constant rate of expansion. The minor radius
 104 is given by

$$105 \quad \text{Minor Radius} = 2(r_0 + A(R - L_0)). \quad (3)$$

106 Interestingly, based on equation (2), by 0.5- 1.0 AU, the predicted aspect ratio tents to a
 107 fixed value. It would mean that the cross section morphology should remain constant.

108 The orientation of the CME (and later of the MC) is also little-understood. Yurchyshyn
 109 [2008] speculates that the axis of the ejecta may rotate towards the heliospheric current
 110 sheet. Rotation in the low corona is observed relatively frequently [Green et al., 2002] but
 111 it was never seen in the outer corona until recently. Vourlidas et al. [2011] provided the
 112 first evidence of a CME rotation in the middle and outer corona.

113 Therefore, analysis of CME images can provide information on the early stages of MCs,
 114 such as the expansion of the CME cross-section, its global structure and the orientation
 115 of the flux rope. This information can then be compared with in situ observations of the
 116 same MC allowing us to better understand the role played by expansion and rotation in
 117 the orientation of the CME at 1 AU. This is very important to accurately forecast the
 118 geo-effectiveness of CMEs.

119 In this paper, we have chosen to analyze the strongly rotating event, on June 16,
 120 2010, reported by Vourlidas et al. [2011] (Paper I, henceforth). It exhibited a very clear
 121 flux-rope structure in the coronagraph and heliospheric imager observations from SEC-

122 CHI/STEREO and LASCO/SOHO, and it was in-situ detected clearly by both MES-
123 SINGER at 0.5 AU and Wind at 1 AU. The event belongs to the class of 'stealth CMEs'
124 [Robbrecht et al., 2009] and therefore it has an extremely weak low corona signatures,
125 no flares, and propagates slowly. The relative locations of the STEREO and MESSEN-
126 GER spacecraft, and Earth (Wind and SOHO) provide a very desirable configuration for
127 analyzing the kinematics and dynamics of this event.

128 For the analysis, we use data from SDO, STEREO, SOHO, Wind and MESSENGER,
129 and several techniques, such as the Graduated Cylindrical Shell (GCS) [Thernisien et
130 al., 2006], and in-situ analytical models with and without distortion in the cross section
131 [Hidalgo et al., 2002; Nieves-Chinchilla et al., 2009; Lepping et al., 1990]. The focus
132 of the paper is the rate of cross-section expansion and distortion of the flux rope, but
133 we will also demonstrate that single view-point observations could lead to confusion in
134 interpreting the observations. Only with the use of multispacecraft/multipoint analysis,
135 we can understand the detailed evolution of these ICMEs.

136 The paper is organized as follows. We present the remote and in-situ observations
137 in § 2 and their analysis in § 3. We offer a set of scenarios that are consistent with
138 the observations in § 4 and discuss the implications for the CME expansion in § 5. We
139 conclude in § 6.

2. Observations of the 16 June, 2010 CME

140 On June 16, 2010, an Earth-directed CME was observed by the STEREO-SECCHI and
141 SOHO-LASCO telescopes. Between June 16 and 21 of 2010, the STEREO spacecraft and
142 Earth (SOHO and Wind spacecraft) are in a configuration such that the angle between
143 Earth and STEREO B (STB) is -70° and between Earth and STEREO A (STA) is 74° .

144 Figure 1 shows the positions of STEREO A and B spacecraft with respect to Earth in the
145 ecliptic plane. The position of the MESSENGER spacecraft also appears in the figure at
146 a distance of ~ 0.5 AU, and at an angle of -20° from the Sun-Earth line towards STB.

2.1. Remote Sensing Observations

147 The CME was observed remotely until it reached Earth on June 21, 7:20 UT. The CME
148 initiation was observed by the EUV imagers aboard three spacecraft; SDO, STA and STB.
149 These and the inner corona observations of the CME are discussed in detail in Paper I.
150 We give only a brief summary here.

151 The CME was first observed in the SECCHI COR1-A and -B fields of view on 16 June
152 2010 at 06:05 UT. The CME was a typical 'stealth CME' event [Robbrecht et al., 2009].
153 It was not associated with any obvious low coronal activity on the disk such as a flare or
154 filament eruption. However, the EUVI-A and B telescopes detected outflowing material,
155 off the Earth-facing solar limb, in 304\AA and 195\AA images. Thanks to the observations,
156 we were able to identify the source region in the SDO/AIA and HMI observations. The
157 event originated from an extended quiet Sun filament channel located close to the cen-
158 tral meridian and oriented at 38° CCW from the solar equator (Figure 2b). A careful
159 inspection of the AIA images revealed a weak post-CME loop arcade after 12:11 UT.

160 Since it was Earth-directed, the CME appeared as a partial-halo in LASCO and had
161 the well-known white light flux rope appearance (e.g., Chen et al. [1997], Vourlidas et al.
162 [2000]) in the SECCHI-A and B coronagraphs. It emerged close to the equator in COR1
163 with a very similar morphology in the COR1-A and B views. However its morphology and
164 location changed significantly as it propagated through the COR2 fields of view, losing
165 some of its symmetry between the A and B views (Figure 2 a-f). The COR2 and HI

166 observations show a clear V structure at the back of the CME which is thought to be
167 indicative of the trailing part of the ejected flux rope [Shiota et al., 2005]. In the COR2
168 and HI1 fields of view, the CME over-expands (Paper I) and flattens from the more
169 circular appearance in COR1. This peculiar behavior is uncommon at these heights but
170 it can be explained by rotation of the structure away from the sky plane without the need
171 to invoke any distortion due to interaction with the solar wind (i.e., 'pancaking'). The
172 observations through the edge of the COR2 field of view are consistent with a rotation
173 rate of 60° per day (Paper I). Table 1 gives the time at which the CME is first observed
174 in each instrument.

2.2. In-situ observations

175 On 21 June 2011 at 7:12 UT, the front of this ICME encountered the Wind spacecraft.
176 At this time, the magnetometer MFI [Lepping et al., 1995] observed a slight increase in the
177 magnetic field magnitude up to a maximum of 8.6 nT, in contrast with the ambient solar
178 wind field of 2.5 nT (Figure 3). A large change was observed in the X-component of the
179 magnetic field that indicates a flux rope topology. The magnetic cloud region is defined by
180 the low proton plasma temperature as measured by the SWE instrument [Ogilvie et al.,
181 1995]. The rear boundary was identified mainly based on the proton plasma temperature
182 profile. The solar wind bulk velocity showed a typical profile for an expanding flux rope.
183 The expansion velocity without any correction was ~ 30 km/s, which according to Owens
184 et al. [2005] is agreement with the transit velocity.

185 On the bottom half of Figure 3, the electron Pitch Angle Distribution (PAD) at 116.1
186 and 193.4 eV show an increase of the electron flux at 0° that suggest magnetic field lines
187 connected to the Sun for one of the CME's legs. This in-situ observation agrees with the

188 remote sensing observations that suggest a disconnection from one of the footpoints (see
189 Paper I).

190 Finally, we point out an increase in electrons at 0° pitch angle inside the magnetic cloud.
191 This increase is associated with a slight increase in the density. However, there does not
192 appear to be any corresponding solar activity at the source region at this time.

193 The MESSENGER mission [Solomon et al., 2001] has become the first mission to orbit
194 around Mercury. The scientific objectives of the MESSENGER mission are not focused
195 on interplanetary or solar studies. However, its proximity to the Sun and its occasional
196 ability to provide an advantageous multispacecraft configuration for some solar transient
197 events has made MESSENGER an important mission for ICME studies. The event here
198 is such an example.

199 Between 19 June 2011 10:05 and 20 June 2011 2:24 UT, the MESSENGER spacecraft
200 was in the ambient solar wind. The onboard magnetometer (MAG), [Anderson et al.,
201 2007], recorded the data in Figure 1. The signatures in the magnetic field magnitude and
202 components show the obvious profile of a flux rope. The MESSENGER mission does not
203 provide plasma parameters, so this event can not be identified as a MC with all certainty,
204 and its boundaries are ambiguous. This fact is important because different time intervals
205 provide different flux-rope orientations and may lead to different scenarios as we will see
206 later.

3. Analysis and Results

207 Our goal is to examine the dynamical evolution during the CME's interplanetary prop-
208 agation in order to understand the heliospheric expansion of these flux ropes. To this
209 end, we have carried out an analysis using a number of different techniques and models

210 available in the literature. Specifically, we have used three methods to obtain information
211 from the data. First, we measured the evolution of the CME envelope as a function of
212 heliocentric distance directly from the images. This so called 'height-time' method pro-
213 vided the rate of expansion of the front with respect to the rear edge. Second, we applied
214 the forward modeling technique of Thernisien et al. [2006] that uses imaging observations
215 from multiple vantage points to derive the orientation, propagation and geometry of the
216 erupting structure at different times. Third, we fitted the in-situ magnetic field data
217 with two analytical models to derive the orientation of the MC. The first model assumed
218 a circular cross-section while the second model allowed possible distortions in the MC
219 cross-section.

3.1. Height-Time Measurements of the CME Envelope

220 This is the most common method of extracting information from HI/coronagraph im-
221 ages through direct measurements of the height versus time of the feature of interest.
222 Because the visible emission is optically thin, these measurements always refer to quan-
223 tities projected onto the plane of the image. Here, we measure four distinct features of
224 the CME: the leading and trailing edges, and the two furthest latitudinal extents of its
225 flanks. We define the trailing edge as the apex of the V-feature (Figure 2). From the
226 measurement of the leading edge, we determine the velocity and position angle of the
227 CME (Table 1). We use these measurements to characterize the dimensions of the CME,
228 by calculating the front elongation and the CME diameters parallel and perpendicular to
229 its propagation. These parameters are represented schematically in Figure 4.

230 Although direct measurements of CMEs are relatively easy to carry out they must be
231 interpreted with care because they are subject to projection effects, which depend on the

232 CME orientation. For example, the perpendicular (to the propagation direction) diameter
 233 is an upper limit to the actual cross-section of the CME. If the CME is oriented face-on,
 234 as in Figure 5a then the perpendicular diameter is the width of the CME. If the CME is
 235 oriented edge-on (Figure 5b), the perpendicular diameter is the actual cross-section of the
 236 CME. For any other orientation between these two extremes, the perpendicular diameter
 237 will be larger than the CME cross-section. Generally, it is difficult to correct for this
 238 projection since we do not know *a priori* how the CME is projected onto the plane of the
 239 sky. A similar argument can be made for the parallel (along the propagation direction)
 240 diameter. Contrary to the case for the perpendicular diameter, the parallel diameter is
 241 the lower bound of the CME cross-section. If the CME is oriented in the plane of the
 242 image then the parallel diameter will be the cross-section. If the CME is oriented out
 243 of the plane of the image then the parallel diameter will be shortened by the projection.
 244 Therefore, the parallel diameter will always be less than or equal to the actual CME
 245 cross-section.

246 The height-time measurements are shown in Figure 6a. They suggest that the expansion
 247 of the CME diameter, whether perpendicular or parallel to the propagation direction, is
 248 not linear. However, we cannot be sure if this is a real or a projection effect until we
 249 correct for projection effects. To properly estimate those, we need to derive the flux-rope
 250 orientation as follows.

3.2. GCS model

251 The Graduated Cylindrical Shell model (GCS) was developed by Thernisien et al.
 252 [2006, 2009] to provide a means for analyzing for 3D morphology, position and kinemat-
 253 ics of CMEs in white-light remote sensing observations. The GCS model uses forward-

254 modeling techniques that allows the user to fit a geometric model of a flux rope to CME
 255 observations. The geometry of the empirical flux rope model is depicted in Figure 5. The
 256 technique allows variation in the Carrington longitude (Φ_{GCS}), heliographic latitude of
 257 the Solar Region (SR, previously identify in Paper I) (Θ_{GCS}) and tilt angle of the SR
 258 neutral line (γ_{GCS}) around the axis of symmetry of the model. The origin is fixed at the
 259 center of the Sun. The size of the flux rope model is controlled by three parameters that
 260 define the apex height, foot point separation and the radius of the outer shell. The main
 261 assumption is the circular cross-section. The details of the model as well as the derivation
 262 of many secondary parameters used in this paper are discussed by Thernisien [2011].

263 The GCS technique has been used to derive the orientation of the flux rope in remote
 264 sensing data and the results agreed well with in-situ observations [Lynch et al., 2010; Ro-
 265 driguez et al., 2011]. We applied this model in Paper I and found that the CME rotates
 266 in the middle corona. Here, we extend the results of Paper I further into interplanetary
 267 space for comparison with the in-situ data. We fit the GCS model to all available coro-
 268 nagraphic images from the time of the CME emergence in the COR1 field of view until
 269 a distance of ~ 0.7 AU in the HI2 images. From the model fit we are able to estimate
 270 the 3D position and size of the CME at each observed height. Figure 6b (top) shows the
 271 ICME direction of propagation and width, derived by the GCS model fitting, projected
 272 to the ecliptic. Figure 6b (bottom) shows the same results projected on a plane normal
 273 to the ecliptic. Our 3D reconstruction suggests that different parts of the CME may have
 274 passed over the MESSENGER spacecraft and Earth.

275 The GCS technique is of limited use for studying CME distortion due to interactions
 276 with the solar wind since the empirically defined flux rope model has a circular cross-

277 section. Regarding the rotation of the structure, we note that, given the symmetry in
 278 the two STEREO views, the third view from LASCO is critical for restricting the CME
 279 orientation. The CME is only visible in the LASCO-C3 data only out to $\sim 32 R_{\odot}$. Thus
 280 the GCS model becomes more uncertain at the distance of MESSENGER to in-situ ob-
 281 servations.

3.3. In-situ analysis

282 Several models have been presented in the literature since Burlaga et al. [1981] defined
 283 magnetic clouds. The MC model developed by Lepping et al. [1990] was the first to
 284 attempt to obtain an understanding of the basic structures although its assumptions are
 285 very restrictive. The Lunquist [1950] solution for a cylindrical approximation for a force-
 286 free torus has represented a framework for the understanding of interplanetary magnetic
 287 cloud. It provides an approach of interpretation for the MC topologies and orientations.
 288 However, by definition, it can not address distortions of the flux rope cross-section.

289 The other analytical model used in this paper was published by Hidalgo et al. [2002]
 290 and further developed by Nieves-Chinchilla et al. [2009]. Two characteristics distinguish
 291 this model from the others in the literature: 1) none force-free condition is assumed, and,
 292 2) an elliptical cylindrical coordinate system is chosen to resolve the Maxwell equations
 293 (Figure 5a in Nieves-Chinchilla et al. [2011]). Both of these conditions significantly relax
 294 the requirements of the model flux rope and allow more general solutions with serious
 295 implications on the global geometry of the fitted ICME. The first condition has implica-
 296 tions for the overall picture of the CME/ICME evolution in the interplanetary medium.
 297 Locally, at 1 AU, the assumption that the system is under a force free condition could be
 298 correct. However, we treat the problem more generally in order to understand the inter-

299 planetary expansion and evolution of the ICME. So we relax the force free condition, in
 300 order to study the evolution of the early stages of the ICME. The second condition has an
 301 impact directly on the structure's geometry. A proper elliptical coordinate system allows
 302 us to consider cross-section distortion. The magnetic field components in this coordinate
 303 system (called MC coordinate system) are obtained under the cylindrical approximation
 304 and are given by

$$305 \quad B_y = B_y^0 - a j_\eta \mu_0 \sinh \eta E[\varphi, -1/\sinh^2 \eta]$$

$$306 \quad B_\varphi = a \mu_0 j_y^0 \frac{\sinh \eta}{\sqrt{\cosh^2 \eta - \cos^2 \varphi}}$$

307 where $E[\varphi, -1/\sinh^2 \eta]$ is the elliptic integral of second kind and it is numerically solved
 308 for in the algorithm [Nieves-Chinchilla et al., 2009]. The characteristics of the parameters
 309 are described by Hidalgo et al. [2002] and Nieves-Chinchilla et al. [2009] for the axial mag-
 310 netic field component (B_y) and poloidal magnetic field component (B_φ). The spacecraft
 311 trajectory inside of the magnetic cloud defines the poloidal angle (φ) around the axial
 312 coordinate (Figure 5b in [Nieves-Chinchilla et al., 2011]), and the focus (a) of the ellipse
 313 that defines the MC cross section. Therefore, model parameters that define the physical
 314 characteristics and MC morphology are: radial and axial current density (j_η, j_0), axial
 315 magnetic field (B_y^0), and distortion (η). Moreover, from the projection of the spacecraft
 316 coordinate system (in this case, RTN coordinates), we are able to get information about
 317 the MC orientation: longitude (ϕ^{model}), latitude (θ^{model}), *local propagation angle* (ξ^{model}),
 318 and the impact parameter (y_0).

319 All fit parameters from the non force-free (NFF) model are included in table 2. The
 320 comparable results from the force-free (FF) model are also included. The angles are
 321 defined as longitude (ϕ^{model}) with the $\phi^{model}=0^\circ$ in the Earth-Sun direction, and, latitude

322 (θ^{model}), from -90° to 90° (where positive values represent north of the ecliptic plane). The
 323 coordinate system is observer-centric. To be consistent with the remote sensing analysis
 324 we define positive values of the CME/ICME axis *tilt* as clockwise rotation around the
 325 Sun-Earth line, centered on the Sun.

326 The purpose of this model is not only to describe the morphology or geometry of the
 327 MC, but also to understand the physics inside of the CME/ICME by relaxing, in this case,
 328 the force free condition. Even though the non-force-free (NFF) model has larger number
 329 of free parameters and thus greater uncertainties, all the fitted parameter correspond
 330 to physical characteristic of the MC that can be tested, such as the local propagation
 331 angle, the direction into which the MC travels. In order to understand the distortion as
 332 a consequence of the interaction of the flux-rope with the ambient solar wind, the in-situ
 333 analysis must take into account that the spacecraft-ICME encounter is not always at the
 334 ICME front and thus, the cross-section major axis is not always perpendicular to the
 335 ecliptic plane (Figure 5b in Nieves-Chinchilla et al. [2011]).

336 In Figure 1, the data from MESSENGER and Wind are shown, along with the NFF
 337 model-fitting (smooth lines). In Table 1, we list the time intervals chosen for this analy-
 338 sis, the solar wind velocity and the maximum magnetic field magnitude in the analysis-
 339 interval. In the case of MESSENGER, the solar wind velocity is an estimated value from
 340 the CME ejection time and ICME arrival time since MESSENGER does not have so-
 341 lar wind instrumentation. Table 2 shows the whole set of fit parameters for the NFF
 342 model and the comparable parameters for the FF model. The obtained orientations for
 343 both models/data are in RTN coordinates. To simplify the interpretation, the Wind data
 344 has also been converted to RTN coordinates using the approximation: $B_x^{GSE} = -B_R$,

345 $B_y^{GSE} = -B_T$, and, $B_z^{GSE} = B_N$, which introduces an error that is significantly less than
 346 the uncertainties of the applied models.

347 Both time intervals selected for the MC boundaries are listed in table 1. In the case of
 348 the MESSENGER observations of this MC, the rear boundary seems to be clear but, we
 349 have at least two possible front boundaries. The results from the model fitting appear in
 350 Table 2. During interval 1 as well as interval 2, the differences in the axis orientation for
 351 the FF and NFF models could be due to the different geometrical approach used by the
 352 models. For interval 1 (shorter), the NFF model gives a longitude ($\phi_{NFF}^{model}=120^\circ$) with a
 353 slight tilt ($\theta_{NFF}^{model}=-38^\circ$). So, for interval 1, the $tilt_{NFF}^{model}$ is 38° from the NFF model, and
 354 with the FF model, we get a slightly different value for the longitude, and the MC's axis
 355 is close to the ecliptic plane ($\phi_{FF}^{model}=128^\circ$ and $tilt_{FF}^{model}=10^\circ$). The schematic picture with
 356 the possible configuration is shown in Figure 7.

357 For the larger interval (interval 2) the front boundary is identified to be earlier, at 3:45
 358 UT of 19 June 2010 (Table 1). The consequences of choosing this earlier start time are
 359 significant. In the case of the FF model, the longitude of the MC axis ($\phi_{FF}^{model}=167^\circ$) and
 360 the latitude ($tilt_{FF}^{model}=69^\circ$) changed significantly compared to the results of the shorter
 361 interval. Likewise, for the NFF model, with a longitude ($\phi_{NFF}^{model}=144^\circ$) and latitude
 362 ($tilt_{NFF}^{model}=43^\circ$), the change is also significant with a diminished goodness of fit. Fur-
 363 thermore, the discrepancies between the results of the two models increases for the second
 364 analysis-interval bringing into question its validity. However, in the case of the axial mag-
 365 netic flux, the result from the FF model is $6.6 \cdot 10^{20}$ Mx and from the NFF model is $4.7 \cdot 10^{20}$
 366 Mx, which is closer to the values obtained at 1 AU, Table 2. The difference between the
 367 two model results is due to the larger cross section area associated with the FF model.

368 We now focus on the Wind observations. Applying the same MC fit procedures, we
 369 found that the *tilt* angle is similar for both models: $tilt_{FF}^{model} = 6^\circ$ and $tilt_{NFF}^{model} = -14^\circ$,
 370 with respect to the ecliptic plane. However, the estimated longitude angles for the models
 371 differ by 32° . For the FF model this implies that the spacecraft could have crossed close
 372 to the front of the MC, but the NFF model results suggest that the spacecraft could have
 373 crossed through the flank. It is important to keep this discrepancy in mind in order to
 374 create a scenario for the CME propagation in the solar wind.

375 One more parameter obtained with the NFF model should be discussed: the distortion
 376 (ϵ), in this case defined as minor axis over the major one. There is a discrepancy between
 377 the analysis results between Interval 1 (on MESSENGER data) with a value of 55%
 378 and Wind with a value of 86%. There is a closer agreement between Wind and the
 379 MESSENGER Interval-2, 86% and 96%, respectively.

4. Remote – In situ Comparisons: CME/ICME Rotation

380 Using on the SECCHI and LASCO remote observations and the Wind in situ data, we
 381 were able to confirm that the June 16 CME was Earth directed. Initially we selected this
 382 event as suitable for studying cross-section expansion because of its well-defined flux-rope
 383 structure in the images, the lack of other interfering events in the interplanetary medium,
 384 and the apparent slight tilt of the ICME on the ecliptic plane. However, we uncovered
 385 several peculiarities as the study progressed.

386 The first peculiarity is related to the lack of a clear source region. This event had the
 387 typical characteristics of 'stealth CMEs' [Robbrecht et al., 2009; Ma et al., 2010]. Only
 388 thanks to the side views from the EUVI telescopes, we were able to identify the source
 389 region and thus determine the orientation of the pre-eruption arcade using PFSS extrap-

390 olations (details on Paper I). The subsequent GCS fits uncover an even more unexpected
391 peculiarity. They showed a large rotation in the middle corona that we were able to fol-
392 low to the location of the MESSENGER in this paper. Figure 8c compares the tilt of
393 the CME/ICME as derived from the remote and in-situ observations. The tilt variation,
394 is measured relative to the solar equator (a positive angle reflects clockwise rotation as
395 viewed from Earth). At the location of MESSENGER, we see that, the tilt angle obtained
396 by the GCS technique differs by $\sim 100^\circ$ from the orientation derived by the analytical
397 in-situ models of the MESSENGER magnetometer data. This is the third peculiarity and
398 we can propose three possible explanations for this discrepancy.

399 1. *CME counter-rotation.* As we have pointed out in Paper I, the CME propagates
400 symmetrically relative to the SECCHI instruments and hence its appearance is very similar
401 from the SECCHI-A or -B viewpoints. We are able to establish the CME rotation reliably
402 thanks to the third eye-views provided by the LASCO coronagraphs. After the CME
403 exits the C3 field of view on June 17th 08:09 UT at a distance of $32 R_\odot$, orientation
404 of the CME from the GCS fit, becomes somewhat ambiguous. Although we can only
405 derive the absolute tilt of the flux rope relative to the plane of symmetry between the
406 STA and STB we cannot tell whether the structure is tilted forward or backward relative
407 to that plane. In Figure 8c we make the straightforward assumption that the CME
408 maintains its counterclockwise rotation after leaving the C3 field of view. But what if
409 the CME decides to oscillate and hence rotate in the opposite sense in the outer corona?
410 Practically speaking, we should be able to see the CME rotating through the 0° by an
411 increase, followed by a decrease, of its latitudinal width. Figure 8b shows the CME width
412 determined by the GCS model and by the perpendicular height-time measurement. It is

413 a fact that the emission at the CME boundaries weakens as it expands making it difficult
 414 to derive the CME orientation with confidence at these large distances. Therefore, it is
 415 conceivable that the CME rotated clockwise between June 17-19. In that case, the tilt in
 416 HI2 would be 55° and would match the MESSENGER in-situ reconstructions very well
 417 (white triangles in Figure 8).

418 To define better this oscillatory scenario, we fitted the values obtained with the GCS
 419 technique until day 17.33 (x_c), to a function:

$$420 \quad angle = A \sin \frac{\pi(x - x_c)}{w} \quad (5)$$

421 where A is the amplitude in the angle equal to 68.0 ± 7.6 , and w is the frequency in
 422 the change of the rotation sense. The value for w parameter is 2.0 ± 0.5 decimal day.
 423 The profile obtained with these parameters is depicted in the Figure 8b with a dash gray
 424 line. The fit matches the MESSENGER in-situ tilt values. Although we do not consider
 425 it further here, we have to accept the 'damped-oscillation' as a viable, and intriguing
 426 scenario for the CME behavior in the heliosphere. Further work should hopefully clarify
 427 this issue.

428 *2. CME keeps rotating.* Alternatively, we can assume that the CME keeps rotating
 429 throughout the HI1 and HI2 fields of view at the same rate as measured in the coronagraph
 430 ($\sim 90^\circ \text{ day}^{-1}$). In that case, the CME would rotate another 180° by the time it reaches
 431 MESSENGER on June 19, 12UT. It will have a tilt of around 90° , which is in relatively
 432 good agreement to the in-situ results.

433 *3. Inaccurate in-situ derived tilts.* Finally, the in-situ reconstructions may be inaccu-
 434 rate. Because the MESSENGER mission does not carry a solar wind plasma instrument
 435 so we are not able to delineate accurately the MC boundaries. However, the MC ori-

436 entation will depend on the chosen boundaries. To account for that, we have tried two
 437 likely intervals and used two analytical models to derive the MC orientation as discussed
 438 in § 3.3.

5. Remote – In situ Comparisons: Expansion

439 After our discussion of the two rotation scenario for our CME, we turn our attention
 440 to the main subject of this paper; namely, the analysis of the evolution of the CME cross
 441 section using the height-time and GCS measurements described in Section 3.1. We are in
 442 the unique position to be able to derive true (deprojected) quantities for the CME cross
 443 sections parallel and perpendicular to its propagation direction because we have three-
 444 dimensional information on the CME size and orientation. First, we derive the deprojected
 445 perpendicular diameter from the diameter determined by the height-time measurements
 446 using the width and *tilt* of the CME from the GCS analysis. The geometry, as viewed
 447 by an observer along the POS, is shown in Figure 8a. The deprojected perpendicular
 448 diameter, D_p^c , is then

$$449 \quad D_p^c = \frac{D_p^d - W \cos \textit{tilt}}{\sin \textit{tilt}} \quad (6)$$

450 where *tilt* is γ^{GCS} and W is the CME width (W , Figure 5). The projected (black circles)
 451 and deprojected (white circles) values are plotted in Figure 8b. Also plotted are the GCS
 452 true (white stars) and projected (black stars) widths. The very small D_p^c values between
 453 June 17-18 are due to the very high inclination ($\sim 90^\circ$) of the CME flux rope which causes
 454 divergence of the correction in equation (5). In other words, we do not have information
 455 on the perpendicular diameter when the CME axis lies on the POS. At later times, the
 456 CME seems to rotate back towards the ecliptic and we can again follow the evolution of

457 D_p^c . However, those later measurements are based on two-viewpoint observations which
 458 introduce some ambivalence on the sign of the CME tilt as we discussed in the previous
 459 section. So, we choose to focus on the more reliable three-viewpoint data (SECCHI +
 460 LASCO) for the analysis of the CME expansion.

461 Figure 9 shows the CME evolution in the inner corona when it was observed by both
 462 SECCHI and LASCO. We present here only the SECCHI-A measurements, since the CME
 463 propagation direction is 20° away from the Sun-Earth line, hence closer to the plane of sky
 464 (POS) of STA (Figure 6b (top)). The measurements cover an 18-hour period, from the first
 465 CME observation to the end of 16 June. From bottom to top, we plot the perpendicular
 466 and parallel diameters, the tilt of the CME derived from the GCS fit, and finally the
 467 ratio of perpendicular to parallel diameters. Note that the perpendicular diameter has
 468 been corrected for the effects of projection and rotation as discussed above. We did not
 469 deproject the parallel diameters since the CME propagates along the SECCHI-A POS and
 470 the projection effects are minimal. The ratio of the two diameters provides a measure of
 471 the distortion of the CME flux rope during its heliospheric propagation. When it is close
 472 to unity, the flux rope has a circular shape. When the distortion ratio is below one, then
 473 the CME is elongated along its propagation direction which is not a common occurrence
 474 in propagation models. Many MHD models of CME propagation predict that the CME
 475 should 'pancake', its distortion should be higher than unity, due to its interaction with
 476 the solar wind and even if it is expanding self-similarly [Riley & Crooker, 2004].

477 At first sight, our projected height-time measurements appear to support that expect-
 478 tation (black circles in Figure 9 top). The (projected) distortion is as high as 1.5 early
 479 on and although it becomes approximately one around day 16.5, it quickly returns above

480 unity. However, the results change as soon as we correct for the projection effects (white
 481 stars). The corrected observations suggest that the flux-rope is distorted mainly in the
 482 propagation direction by as much as a factor of two more than in the perpendicular di-
 483 rection. It seems, therefore, that projection effects can affect significantly the analysis of
 484 imaging observations based on 'point-and-click' methods, such as height-time measure-
 485 ments. Every effort should be made to estimate the three-dimensional configuration of
 486 the structures and to attempt projection corrections before reaching any conclusions.

487 We now return our attention to the variation of the two diameters, parallel and per-
 488 pendicular. We fit the measurements between June 16 and 17 (Figure 9 as a function of
 489 heliocentric distance using equation (1), where x is the heliocentric distance. Then we
 490 extrapolate that function to distances beyond 1 AU to compare with the other imaging
 491 measurements and the in-situ models. The results are plotted in Figure 10 with red lines.
 492 We also plot the Bothmer & Schwenn [1998] empirical law (blue lines) for comparison.
 493 In the same figure, we plot the projected and corrected height-time measurements (black
 494 dots and white stars, respectively), the predicted perpendicular diameters based on the
 495 Savani et al. [2011] results (orange dots) and finally, the values obtained from the analyt-
 496 ical in-situ models at 0.5 and 1 AU (red/green/blue symbols for different time intervals,
 497 see also Tables 1 and 2).

498 The conclusions are straightforward in the case of the parallel diameter. We find a rate
 499 of expansion, $D_{par} = 0.20 \pm 0.04x^{0.74 \pm 0.02}$, very similar to Bothmer & Schwenn [1998] and
 500 Savani et al. [2009]. Our results agree very well with the NFF model with Interval-2 for
 501 both MESSENGER (at 0.5 AU) and Wind (at 1 AU).

502 In the case of the perpendicular diameter, the agreement among the various models is
 503 less satisfactory. It is clear that the projected height-time measurements and the Savani et
 504 al. [2011] results, which are based on projected measurements are inconsistent with both
 505 in-situ models and the empirical law. This is hardly surprising since we have established
 506 that projected quantities are unreliable. Indeed, the deprojected measurements produce
 507 a fit, $D_{perp} = 0.15 \pm 0.04x^{0.89 \pm 0.09}$, consistent with the Interval-2 NFF model for MES-
 508 SENDER and consistent with the corrected measurements in the HI1 and 2 fields of view
 509 (which we choose not to include in the fit). At 1 AU our expansion fit predicts a smaller
 510 diameter than the in-situ models. We do not know the reason for this discrepancy. It may
 511 be that a single exponent is not a good description for the evolution of the perpendicular
 512 diameter in the inner heliosphere. The deprojected measurements around 0.5 AU suggest
 513 a sharper slope than 0.89, for example. Alternatively, Wind could be crossing a different
 514 part of the CME compared to MESSENGER which in turn may be expanding at a differ-
 515 ent rate. The imaging measurements are unlikely to be sensitive to such intra-structure
 516 variations because of the large line of sight integration.

517 Finally, we should clarify how we use equations 2 and 3 from Savani et al. [2011] to
 518 obtain a prediction for the variation of the perpendicular diameter. The minor radius in
 519 Savani et al. [2011] corresponds to our parallel diameter. Since their parallel diameter is
 520 consistent with our results and the Bothmer & Schwenn [1998] empirical relationship, we
 521 can use it to obtain the rate of expansion, A , from equation 3. Adopting the standard
 522 values for r_0 and L_0 (see section § 1), we find $A=0.115$. According to Savani et al. [2011],
 523 this value suggests that the perpendicular diameter (their major diameter) is five times
 524 larger than the minor diameter. Although these values (orange circles in Figure 10) are in

525 agreement with Owens [2006] and Forsyth et al. [2006], they are in obvious disagreement
526 with both our corrected results and with the in-situ analytical models. The reason is
527 obvious: projection effects must be taken into account for any measurements extracted
528 from imaging observations.

6. Summary and Conclusions

529 In this paper, we investigate the rate of expansion of a CME both parallel and perpen-
530 dicular to its direction of propagation. We use imaging observations from the SOHO and
531 STEREO spacecraft, magnetometer data from the MESSENGER mission and a complete
532 set of plasma and magnetic field data from the Wind spacecraft. Thanks to the resulting
533 comprehensive coverage, we are able to track the CME from its origin on June 16 to its
534 impact on Earth on June 21, 2010 and derive its three-dimensional properties during that
535 time interval. We selected this event because it was Earth-directed, and belonged to the
536 class of 'stealth CMEs' which may be of interest to the space weather community.

537 The spatial configuration of these spacecraft allow us to link the remote observations
538 to the in-situ data through the use of direct measurements and 3D reconstructions based
539 on multipoint imaging and analytical in-situ models. This event, which initially appears
540 to be a normal fluxrope-type CME, actually provides the first unambiguous evidence of
541 CME rotation in the middle corona. The serendipity of the measured rotation ($100^\circ/\text{day}$)
542 necessitated a separate publication (Paper 1) and remains unexplained. To complicate
543 matters, when the event was detected by MESSENGER as a MC, its orientation based
544 on the in-situ measurements was 100° away from the orientation based on the imaging
545 analysis. However, the imaging-derived orientation may have a sign ambiguity relative to
546 the plane of symmetry of the SECCHI instruments. In Section 4, we offer two possible

547 explanations for this discrepancy: either (1) the CME continues to rotate at the same rate
548 throughout its journey to 0.5 AU, or (2) the CME rotates back towards its pre-eruption
549 orientation. Either scenario is plausible at this stage since we lack any other similar events
550 to compare with. Theoretical modeling cannot guide us either. We are not aware of any
551 CME propagation models that have looked at the effects of CME rotation or oscillation
552 in the interplanetary space. Regarding the ability of this event to rotate so much, we can
553 only point to the observation of disconnection of one of the CME legs (Paper I) that may
554 have allowed the large-scale flux rope to rotate in the observed manner. Certainly, future
555 modeling of this event will shed some light on which of the two scenario is more plausible.

556 Thanks to the three-dimensional information on the CME shape, the analysis of the
557 CME cross section expansion, the main focus of our paper, can be corrected for the large
558 rotation. Using a 'point-and-click' method, we obtain the parallel and perpendicular
559 diameter (relative to the propagation plane) as a function of time and heliocentric distance.
560 We then deproject this quantities using the tilt and width provided by the GCS fits to
561 the structure. Our results can be summarized as follows:

- 562 • The distortion, defined as the ratio of the perpendicular to the parallel projected
563 diameters, results in an elliptical shape consistent with model predictions of a pancaking
564 CME. However, this picture changes completely once the measurements are corrected for
565 projection effects. The corrected values show a distortion along the propagation plane, a
566 'stretching' of the CME, indicating, perhaps, a high-beta structure interaction with the
567 ambient wind.

- 568 • The 3D analysis shows that the CME propagates close to the STEREO-A POS and
569 hence the parallel diameter should not suffer projection effects. Indeed, we find that our

570 fit to the parallel diameter evolution as a function of distance is in very good agreement
571 to the same in-situ model for 0.5 AU (MESSENGER) and 1 AU (Wind) and with the
572 the empirical relationship of Bothmer & Schwenn [1998] for the interval of 0.3 to 4.5 AU.
573 Hence, our analysis extends the validity of their model to about 5 solar radii.

574 • The perpendicular diameters need to be corrected for projection effects. As for the
575 parallel diameter, we find that the rate of expansion agrees very well with the NFF
576 model at MESSENGER but underpredicts at Wind. When comparing to the in-situ
577 analytical models, we must point out that the Wind and MESSENGER spacecraft could
578 be crossing different parts of the MC. Therefore, the discrepancy may indicate a varying
579 rate of expansion at different CME locations or it may reflect a change in the expansion
580 rate after 0.5 AU. There is a slight indication of the latter in the imaging measurements
581 around 0.5 AU (Figure 10).

582 • Our rate of perpendicular expansion is slightly different from the Bothmer & Schwenn
583 [1998] results. This discrepancy is probably unsurprising since Bothmer & Schwenn [1998]
584 had no information on the latitudinal shape of the events in their analysis. They had to
585 assume a constant circular shape. However, the SECCHI imaging observations since
586 the launch of STEREO clearly show that the CME cross-section does not typically stay
587 constant. The imaging analysis reported here suggests that the shape of the cross section
588 can vary from elliptical to circular and back to elliptical as a function of heliocentric
589 distance.

590 • Finally, our analysis does not provide evidence for CME pancaking away from the
591 ecliptic plane despite model predictions. For example, Riley & Crooker [2004] predicts a
592 progressive flattening in the perpendicular (to the ecliptic plane) direction with increasing

593 heliocentric distance. Our results are also in disagreement with geometrical arguments
594 from Savani et al. [2011]. Their predictions fare worse than our own measurements. The
595 Savani et al. [2011] equations predict a much faster expansion rate than observed either
596 by the imaging instruments or derived from the in-situ data. This does not mean that
597 pancaking does not take place during CME propagation. Our detailed investigation of the
598 CME three-dimensional properties (direction, shape, tilt, and width) suggests, however,
599 that the appearance of pancaking structures in images may be the results of projection
600 effects, including CME rotation.

601 It is clear that further research is required to understand the latitudinal expansion of
602 CMEs. In our case, the discrepancy between imaging and in-situ measurements is most
603 pronounced during the last 0.5 AU of transit of the ICME to Earth. This discrepancy
604 could be due to: 1) the projection effects are still not understood, and, 2) the Wind
605 spacecraft is crossing different parts of the MC. Furthermore, the dynamic interaction
606 with the ambient solar wind on the flanks could be different from the MC front [Odstreil
607 & Pizzo, 1999].

608 The analysis of the CME event on June 16th provided an opportunity to combine the
609 remote observations and in-situ data with different techniques and analytical models.
610 Thanks to the multi-viewpoint observations we were able to uncover unexpected behavior
611 (rotation) and account for it in our analysis. We present the first deprojected measure-
612 ments of the variation of the CME size in the inner heliosphere. The results suggest
613 that the parallel expansion obtained with data analysis techniques, models and geometri-
614 cal predictions are in very good agreement. However, the evolution of the perpendicular
615 expansion is still unclear. It is encouraging that the analysis done with the imaging obser-

616 vations, including corrections using the GCS technique, agrees with the in-situ analytical
617 analysis. This result suggests that a combination of remote and in-situ observations has
618 the potential to understand the dynamical interaction of CMEs with the solar wind and
619 could be possible lead to the development of an analytical model. But first, our initial
620 results need to be corroborated with a survey of events.

621 **Acknowledgments.** The work of R.C and A.V is supported by NASA contract S-
622 13631-Y. SOHO is an international collaboration between NASA and ESA. LASCO was
623 constructed by a consortium of institutions: NRL (USA), MPS (Germany), LAM (France)
624 and Univ. of Bham (Birmingham, UK). The SECCHI data are produced by an interna-
625 tional consortium of the NRL, LMSAL and NASA GSFC (USA), RAL and Univ. Bham
626 (UK), MPS (Germany), CSL (Belgium), IOTA and IAS (France).

627 Anderson, B. J., Acuña, M. H., Lohr, D. A., Scheifele, J., Raval, A., Korth, H., & Slavin,
628 J. A. (2007), The magnetometer instrument on MESSENGER, *Space Sci. Rev.*, 131(14),
629 417- 450, doi:10.1007/s11214-007-9246-7.

630 Bothmer, V., & Schwenn, R. (1998), The structure and origin of magnetic clouds in the
631 solar wind, *Ann. Geophys.*, 16, 1- 24, doi:10.1007/s00585- 997-0001-x.

632 Burlaga, L., Sittler, E., Mariani, F., & Schwenn, R. (1981), Magnetic loop behind an
633 interplanetary shock, *J. Geophys. Res.*, 86, 6673- 6684, doi:10.1029/JA086iA08p06673.

634 Burlaga, L. F. (1988), Magnetic Clouds and Force-Free Fields with Constant Alpha, *J.*
635 *Geophys. Res.*, 93(A7), 7217- 7224, doi:10.1029/JA093iA07p07217.

636 Chen, J., Howard, R. A., Brueckner, G. E., et al. (1997), Evidence of an erupting magnetic
637 flux rope: LASCO coronal mass ejection of 1997 April 13, *Astrophys. J.*, 490, L191.

638 Forsyth, R. J., Bothmer, V., Cid, C., et al. (2006), ICMEs in the inner heliosphere: Ori-
639 gin, evolution and propagation effects, *Space Sci. Rev.*, 123, 383- 416, doi:10.1007/s11214-
640 006-9022-0.

641 Gosling, J. T., Bame, S. J., McComas, D. J., & Phillips, J. L. (1990), Coronal mass
642 ejections and large geomagnetic storms, *Geophys. Res. Lett.*, 17(7), 901- 904.

643 Green, L. M., López fuentes, M. C., Mandrini, C. H., et al. (2002), The Magnetic Helicity
644 Budget of a cme-Prolific Active Region, *Solar Phys*, 208, 43.

645 Hidalgo, M. A., Nieves-Chinchilla, T., & Cid, C. (2002), Elliptical cross-section model
646 for the magnetic topology of magnetic clouds, *Geophys. Res. Lett.*, 29(13), 1637,
647 10.1029/2001GL013875, 2002.

648 Hidalgo, M. A., Blanco, J. J., Alvarez, F. J., & Nieves-Chinchilla, T. (2011), On
649 the relationship between magnetic clouds and the great geomagnetic storms associ-
650 ated with the period 1995-2006, *J. Atmos. Sol. Terr. Phys.*, 73, 1372- 1379.
651 dx.doi.org/10.1016/j.jastp.2011.02.017.

652 Hidalgo, M. A. & Nieves-Chinchilla, T., A global magnetic topology model for magnetic
653 clouds (I). Accepted for *Astrophysical Journal*.

654 Howard, R. A., Moses, J. D., Vourlidas, A., et al. (2008), Sun Earth Connection Coro-
655 nal and Heliospheric Investigation (SECCHI), *Space. Sci. Rev.*, 136(1- 4), 67- 115,
656 doi:10.1007/s11214-008-9341-4.

657 Hu, Q., & Sonnerup, B. U. Ö. (2002), Reconstruction of magnetic clouds in the
658 solar wind: Orientations and configurations, *J. Geophys. Res.*, 107(A7), 1142,
659 doi:10.1029/2001JA000293.

660 Kaiser, M. L., Kucera, T. A., Davila, J. M., et al. (2008), The STEREO Mission: An
661 Introduction, *Space Sci. Rev.*, 136, 516, doi:10.1007/s11214-007-9277-0.

662 Lepping, R. P., Burlaga, L. F., & Jones, J. A. (1990), Magnetic field structure of inter-
663 planetary magnetic clouds at 1 AU, *J. Geophys. Res.*, 95(A8), 11,957.

664 Lepping, R. P., et al. (1995), The Wind Magnetic Field Investigation, *Space Sci. Rev.*,
665 71, 207- 229.

666 Lundquist, S., Magnetohydrostatic fields, *Ark., Fys.*, 2, 361, 1950.

667 Lynch, B. J., Antiochos, S. K., Li, Y., Luhmann, J. G., & DeVore, C. R. (2009), Rotation
668 of Coronal Mass Ejections during Eruption, *Astrophys. J.*, 697, 1918.

669 Lynch, B. J., Li, Y., Thernisien, A. F. R., Robbrecht, E., Fisher, G. H., Luhmann, J. G.,
670 & Vourlidas, A. (2010), Sun to 1 AU propagation and evolution of a slow streamer-blowout
671 coronal mass ejection, *J. Geophys. Res.*, 115, A07106, doi:10.1029/2009JA015099.

672 Ma, S., Attrill, G. D. R., Golub, L., & Lin, J. (2010), Statistical Study of Coronal Mass
673 Ejections With and Without Distinct Low Coronal Signatures, *Astrophys. J.*, 722, 289.
674 doi:10.1088/0004-637X/722/1/289.

675 Möstl, C., Miklenic, C., Farrugia, C. J., Temmer, M., Veronig, A., Galvin, A. B., Vršnak,
676 B., & Biernat, H. K. (2008), Two-spacecraft reconstruction of a magnetic cloud and
677 comparison to its solar source, *Ann. Geophys.*, 26, 3139- 3152, doi:10.5194/angeo-26-
678 3139-2008.

679 Möstl, C., et al. (2009), Multispacecraft recovery of a magnetic cloud and its
680 origin from magnetic reconnection on the Sun, *J. Geophys. Res.*, 114, A04102,
681 doi:10.1029/2008JA013657.

682 Nieves-Chinchilla, T., Viñas, A.-F., &Hidalgo, M. A. 2009, Magnetic Field Profiles
683 Within Magnetic Clouds: A Model-Approach, *Earth Moon and Planets*, 104, 109.

684 Nieves-Chinchilla, T., et al. (2011), Analysis and study of the in situ observa-
685 tion of the June 1st 2008 CME by STEREO, *J. Atmos. Sol. Terr. Phys.*
686 doi:10.1016/j.jastp.2010.09.026, 73, 1348.

687 Odstrcil, D., & Pizzo, V. J. (1999), Distortion of the interplanetary magnetic field by
688 three-dimensional propagation of coronal mass ejections in a structured solar wind, *J.*
689 *Geophys. Res.*, 104, 28,225- 28,239, doi:10.1029/1999JA900319.

690 Ogilvie, K. W., et al. (1995), SWE, A Comprehensive Plasma Instrument for the Wind
691 Spacecraft, *Space Sci. Rev.*, 71(14), 5577, doi:10.1007/ BF00751326.

692 Owens, M. J., Cargill, P. J., Pagel, C., Siscoe, G. L., & Crooker, N. U. (2005), Charac-
693 teristic magnetic field and speed properties of interplanetary coronal mass ejections and
694 their sheath regions, *J. Geophys. Res.*, 110, A12105, doi:10.1029/2005JA011343.

695 Owens, M. J. (2006), Magnetic cloud distortion resulting from propagation through
696 a structured solar wind: Models and observations, *J. Geophys. Res.*, 111, A12109,
697 doi:10.1029/2006JA011903.

698 Richardson, I. G., Cane, H. V., & Cliver, E. W. 2002. Sources of geomagnetic ac-
699 tivity during nearly three solar cycles (1972-2000). *J. Geophys. Res.*, 107(A8), 1187,
700 doi:10.1029/2001JA000504.

701 Riley, P., & Crooker, N. U. (2004), Kinematic Treatment of Coronal Mass Ejection
702 Evolution in the Solar Wind, *Astrophys. J.*, 600, 1035.

703 Riley, P., Linker, J. A., Lionello, R., et al. 2004, Fitting flux ropes to a global MHD
704 solution: a comparison of techniques, *J. Atmos. Sol. Terr. Phys.*, 66, 1321.

- 705 Robbrecht, E., Patsourakos, S., & Vourlidas, A. (2009), No Trace Left Behind: STEREO
706 Observation of a Coronal Mass Ejection Without Low Coronal Signatures, *Astrophys. J.*,
707 701, 283.
- 708 Rodriguez, L., Mierla, M., Zhukov, A. N., West, M., & Kilpua, E. (2011), Linking
709 Remote-Sensing and In Situ Observations of Coronal Mass Ejections Using STEREO,
710 *Sol. Phys.*, 270, 561
- 711 Shiota, D., Isobe, H., Chen, P. F., et al. (2005), Self-Consistent Magnetohydrodynamic
712 Modeling of a Coronal Mass Ejection, Coronal Dimming, and a Giant Cusp-shaped Arcade
713 Formation, *Astrophys. J.*, 634, 663678, doi:10.1086/496943.
- 714 Solomon, S. C., et al. (2001), The MESSENGER mission to Mercury: scientific objectives
715 and implementation, *Planet. Space Sci.*, 49(14- 15), 1445- 1465.
- 716 Savani, N. P., Rouillard, A. P., Davies, J. A., et al. (2009), The radial width of a Coro-
717 nal Mass Ejection between 0.1 and 0.4 AU estimated from the Heliospheric Imager on
718 STEREO, *Ann. Geophys.*, 27(11), 4349- 4358.
- 719 Savani, N. P., Owens, M. J., Rouillard, A. P., Forsyth, R. J., Kusano, K., Shiota, D.,
720 & Kataoka, R. (2011), Evolution of Coronal Mass Ejection Morphology with Increasing
721 Heliocentric Distance. I. Geometrical Analysis, *Astrophys. J.* 731, 109.
- 722 Schrijver, C. .J (2001), Simulations of the Photospheric Magnetic Activity and Outer
723 Atmospheric Radiative Losses of Cool Stars Based on Characteristics of the Solar Magnetic
724 Field, *Astrophys. J.*, 547, 475.
- 725 Thernisien, A. F. R., Howard, R. A., & Vourlidas, A. (2006), Modeling of Flux Rope
726 Coronal Mass Ejections, *Astrophys. J.*, 652, 763.

- 727 Thernisien, A., Vourlidas, A., & Howard, R. A. (2009), Forward Modeling of Coronal
728 Mass Ejections Using STEREO/SECCHI Data, *Sol. Phys.*, 256, 111.
- 729 Thernisien, A. (2011), Implementation of the Graduated Cylindrical Shell Model for the
730 Three-dimensional Reconstruction of Coronal Mass Ejections, *The Astrophys. J. Supp.*
731 *S.*, 194:33 (6pp), doi:10.1088/0067-0049/194/2/33.
- 732 Vourlidas, A., Subramanian, P., Dere, K. P., & Howard, R. A. (2000), Large-angle spec-
733 trometric coronagraph measurements of the energetics of coronal mass ejections, *Astro-*
734 *phys. J.*, 534, 456467.
- 735 Vourlidas, A., Colaninno, R., Nieves-Chinchilla, T., & Stenborg, G. (2011), The First Ob-
736 servation of a Rapidly Rotating Coronal Mass Ejection in the Middle Corona, *Astrophys.*
737 *J. Lett.*, 733, L23- L28, doi:10.1088/2041- 8205/733/2/L23.
- 738 Yashiro, S., Gopalswamy, N., Michalek, G. St. Cyr, O. C., Plunkett, S. P., Rich, N. B.,
739 & Howard, R. A. (2004), A catalog of white light coronal mass ejections observed by the
740 SOHO spacecraft, *J. Geophys. Res.*, 109, A07105, doi:10.1029/2003JA010282.
- 741 Yurchyshyn, V. (2008), Relationship between EIT Posteruption Arcades, Coronal Mass
742 Ejections, the Coronal Neutral Line, and Magnetic Clouds, *Astrophys. J.*, 675, L49.

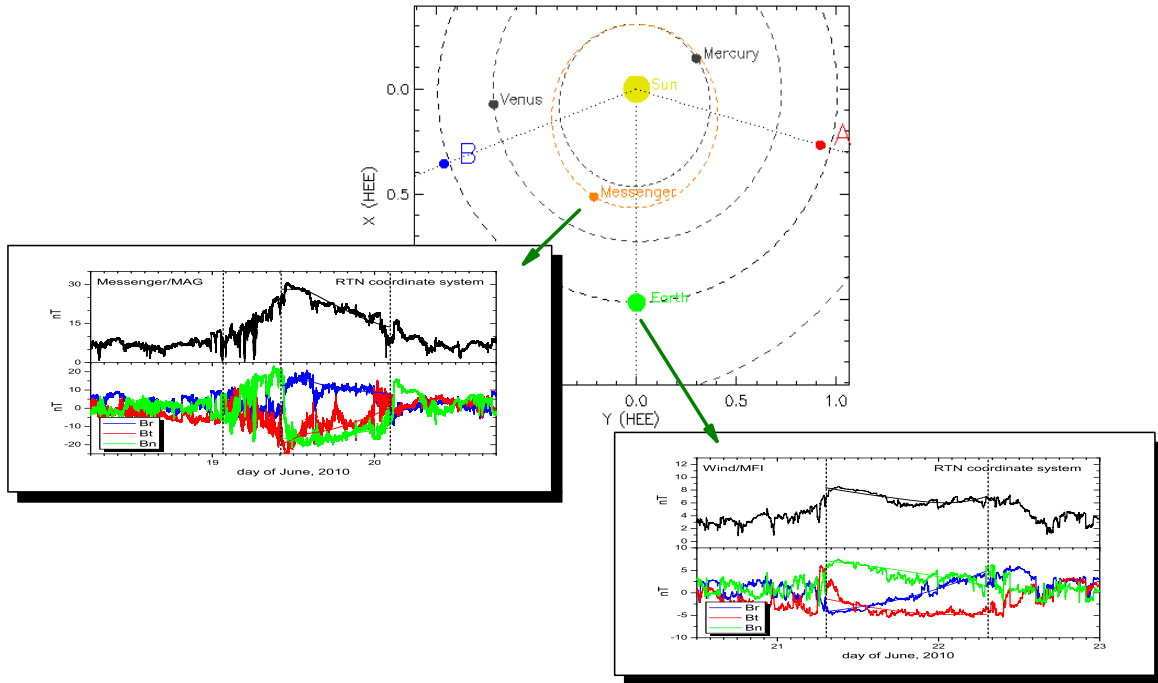


Figure 1. In the center, the positions of the STEREO A (red), STEREO B (blue), MESSENGER (orange), and Earth (green) depicted in the ecliptic plane on 16 June 2010. These missions provide us the data collected for the multipoint analysis of the single CME of June 16, 2010. The STEREO A and B spacecraft are at -74° and 70° from Earth, respectively. The MESSENGER spacecraft is at $r \sim 0.5$ AU and at a -20° angle with respect to the Earth-Sun line. SOHO and Wind are near Earth. Indicated with green arrows, two different set of panels for the in-situ magnetic field magnitude and components data and fitting with the NFF model are shown. On the bottom, from the Wind/MFI instrument and, on the left, the MESSENGER/MAG instrument.

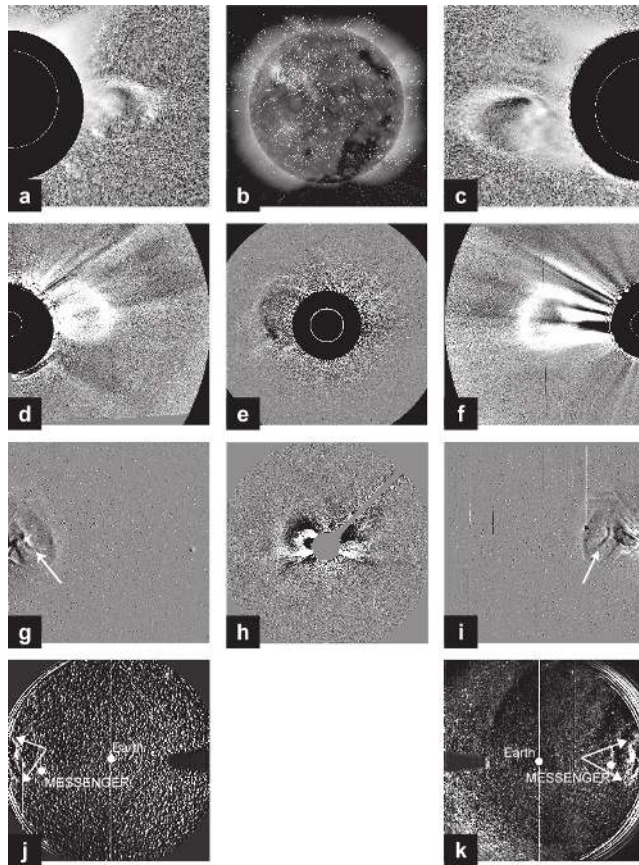


Figure 2. The left, center and right columns show images from the perspective of STEREO B, Earth, and STEREO A, respectively. (a, c) SECCHI COR1 images at 2010 June 16 12:10 UT. The CME emerging from a southern source region. (b) SDO AIA 193Å image at 2010 June 16 23:55:30 UT with superimposed field lines from a PFSS extrapolation. The CME source region is located mid-disk in the Southern hemisphere. (d, f) SECCHI COR2 images at 2010 June 16 18:24 UT. The CME has lost some of its symmetry from COR1 indicating non-radial motion. (e) LASCO C2 image at 2010 June 16 18:27 UT. LASCO images are critical for accurately obtaining the CME orientation. (g, i) SECCHI HI-1 images at 2010 June 17 09:29 UT. The CME front appears flattened with an elliptical cross-section. (h) LASCO C3 image at 2010 June 17 09:17 UT. The CME is expanding predominately to the north following a non-radial propagation path. (j, k) SECCHI HI-2 images at 2010 June 18 18:09 showing the CME front (highlighted with arrows) in relation to MESSENGER and EARTH.

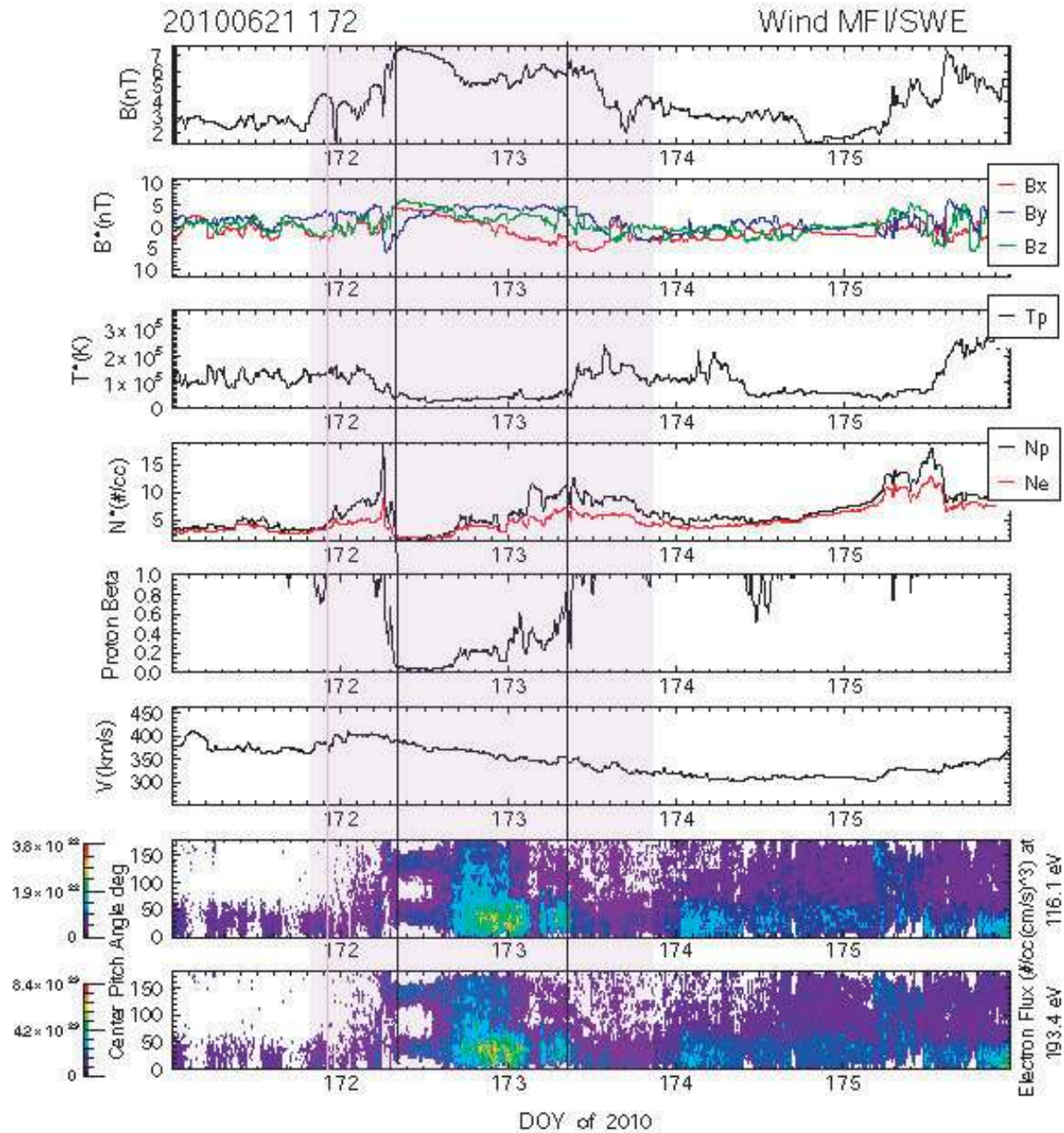


Figure 3. In-situ data from the MFI and SWE instruments onboard the Wind spacecraft. From the top, the magnetic field components and magnitude, proton plasma temperature and density, the solar wind bulk velocity. Below, the electron pitch angle distribution for different energy levels are shown. The vertical black lines mark the interval of the MC.

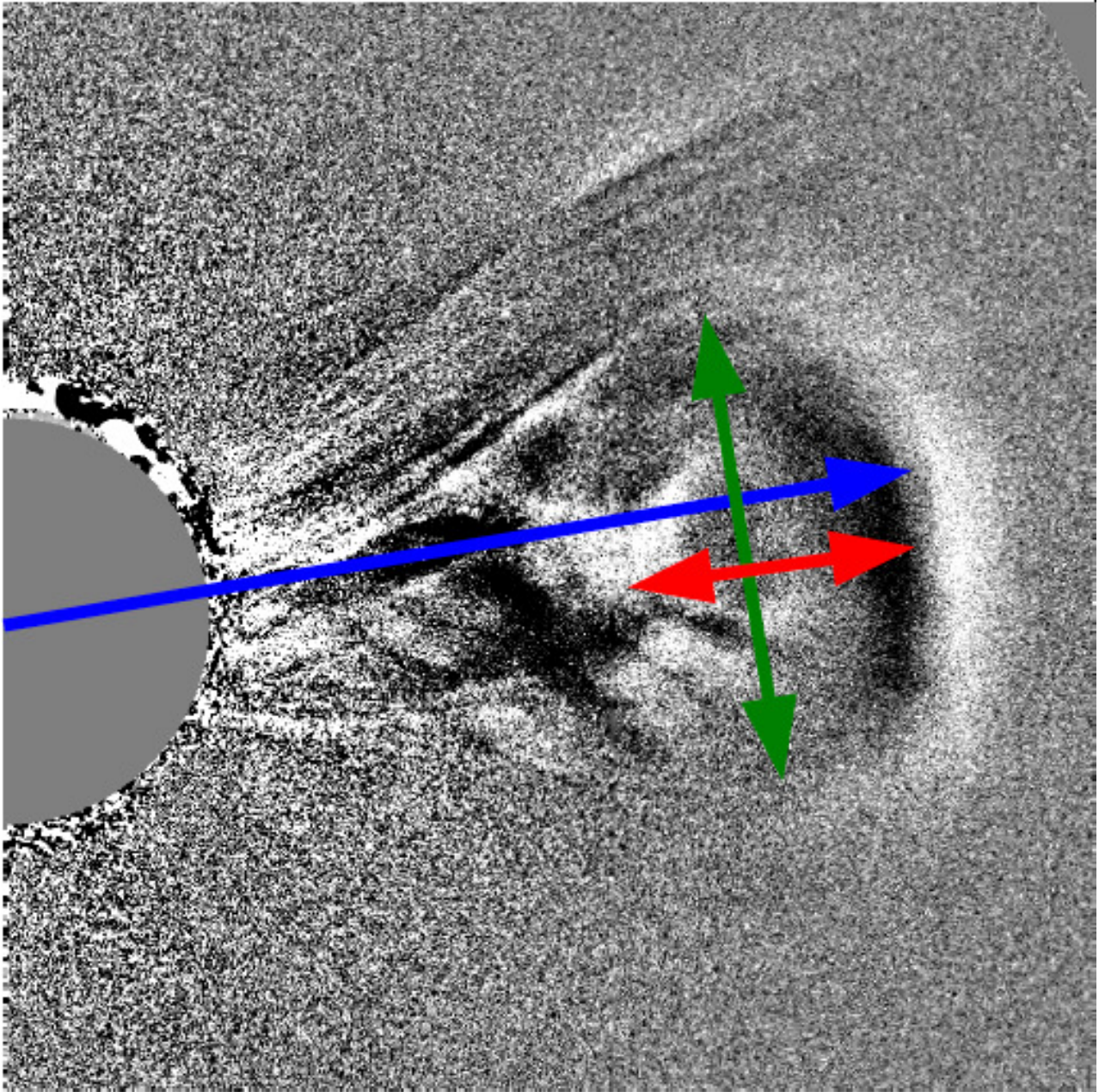


Figure 4. Image taken by STEREO A COR2 of the studied CME over-plotted with a schematic representation of the three direct measurements we made: blue -elongation; red - parallel CME cross-section diameter; and green - perpendicular CME cross-section diameter.

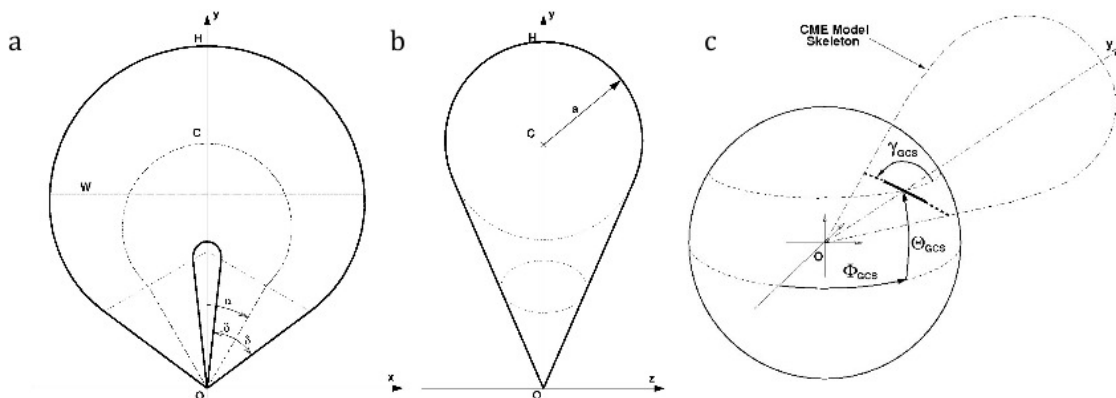


Figure 5. Representation of the graduated cylindrical shell (GCS) model (a) face-on, (b) edge on, and (c) the 3D representation. The dash-dotted line is the axis through the center of the shell. The solid line represents a planar cut through the cylindrical shell at the origin. The width (W) of the model is defined as the largest vertical extent, dotted line. The radius, a , defines the circular cross-section. These values are controlled by the model fitting parameters: height (H), the Carrington longitude (ϕ_{GCS}), heliographic latitude (θ_{GCS}), and the tilt angle (γ_{GCS}) [Thernisien et al., 2009].

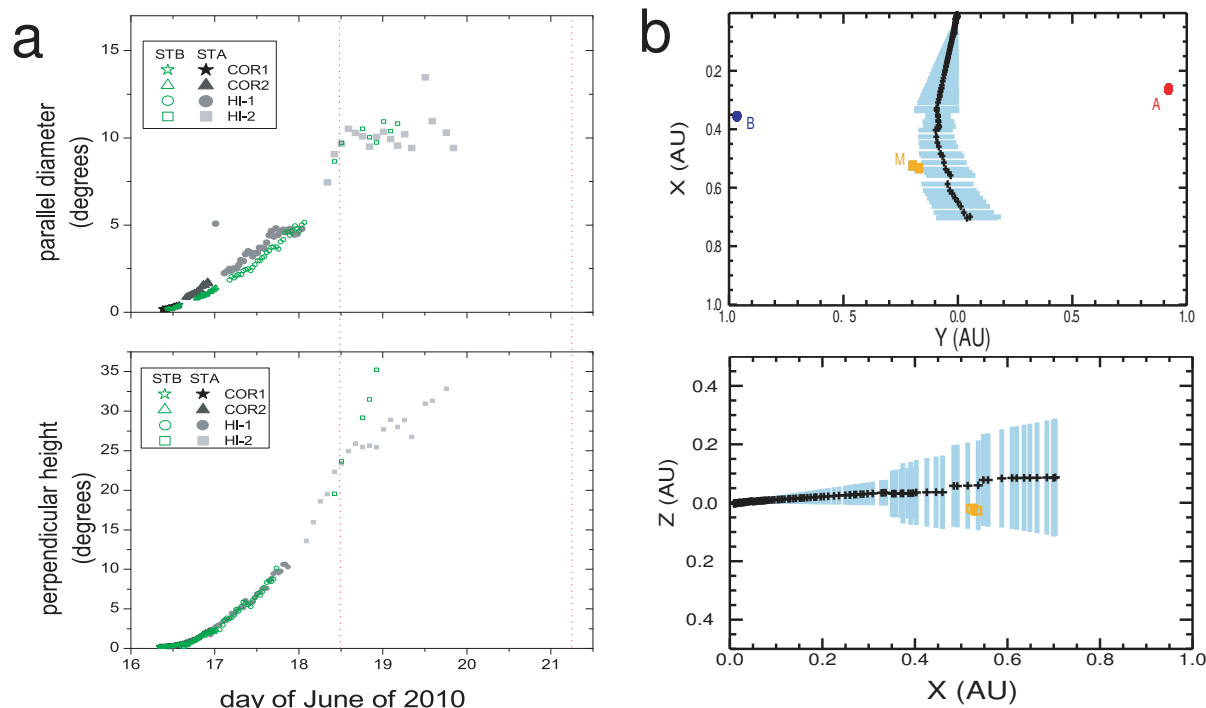


Figure 6. a) Shows the parallel (top) and perpendicular (bottom) diameters obtained from height-time measurement of the data from the STEREO A and B SECCHI sets of instruments. The dotted vertical lines mark when the in situ spacecraft detected the front of the ICME. b) Shows the results of the CGS model fitting of the CME. On the top, the sequence projected onto the ecliptic plane. The plus signs indicate the apex of the model and the blue lines provide the projected extent of the model fit. The positions of the STEREO A and B spacecraft and MESSENGER spacecraft are shown by red, blue and orange dots, respectively. On the bottom, the sequence projected onto the Sun-Earth plane. Orange dot is the MESSENGER spacecraft position and Earth is at the (1,0,0) position.

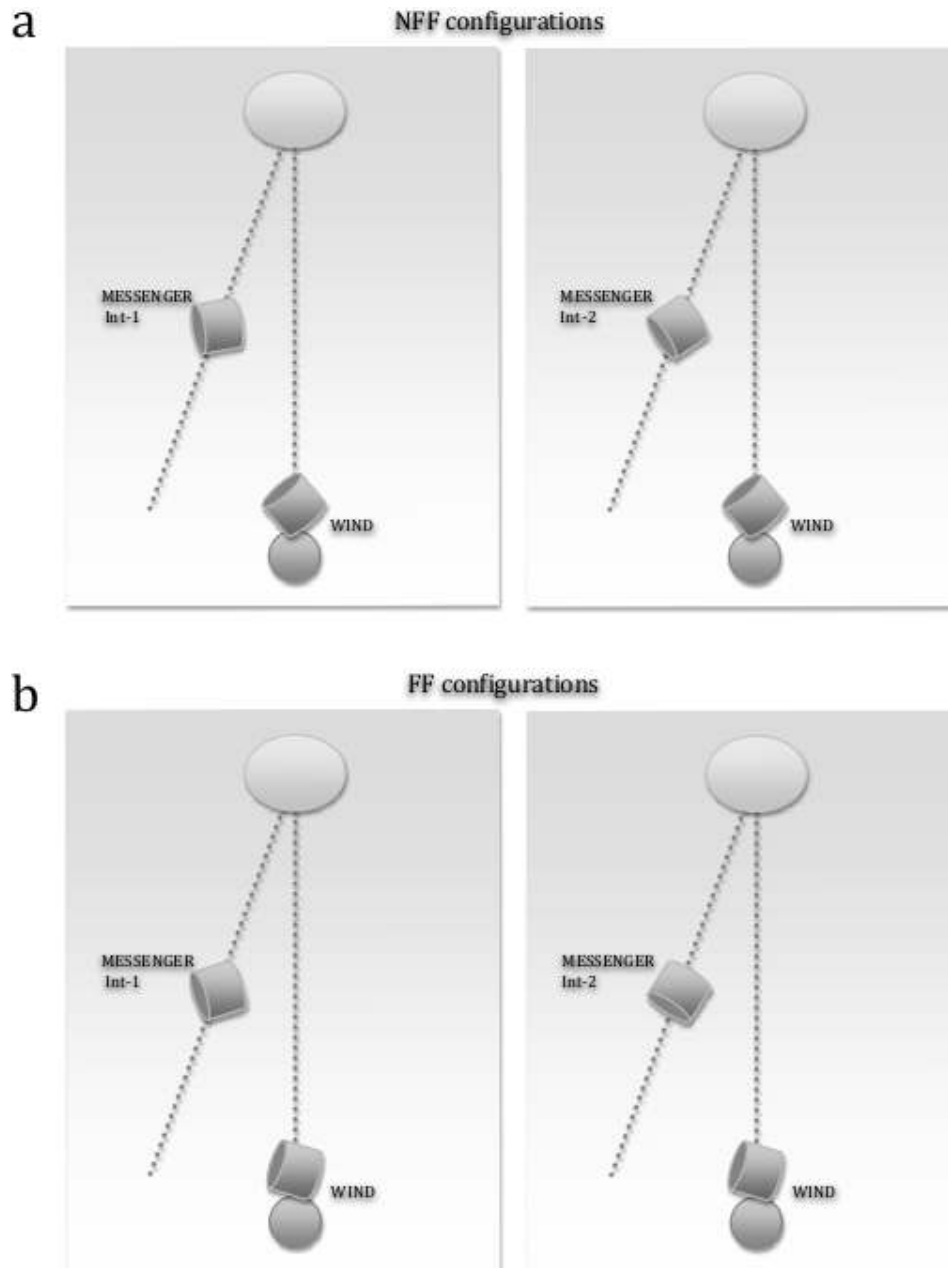


Figure 7. The possible configurations on the ecliptic plane for the MC evolution as predicted by the in situ analytical models a) FF= Force Free, and b) NFF = Non Force Free. The detailed values are in the Table 2.

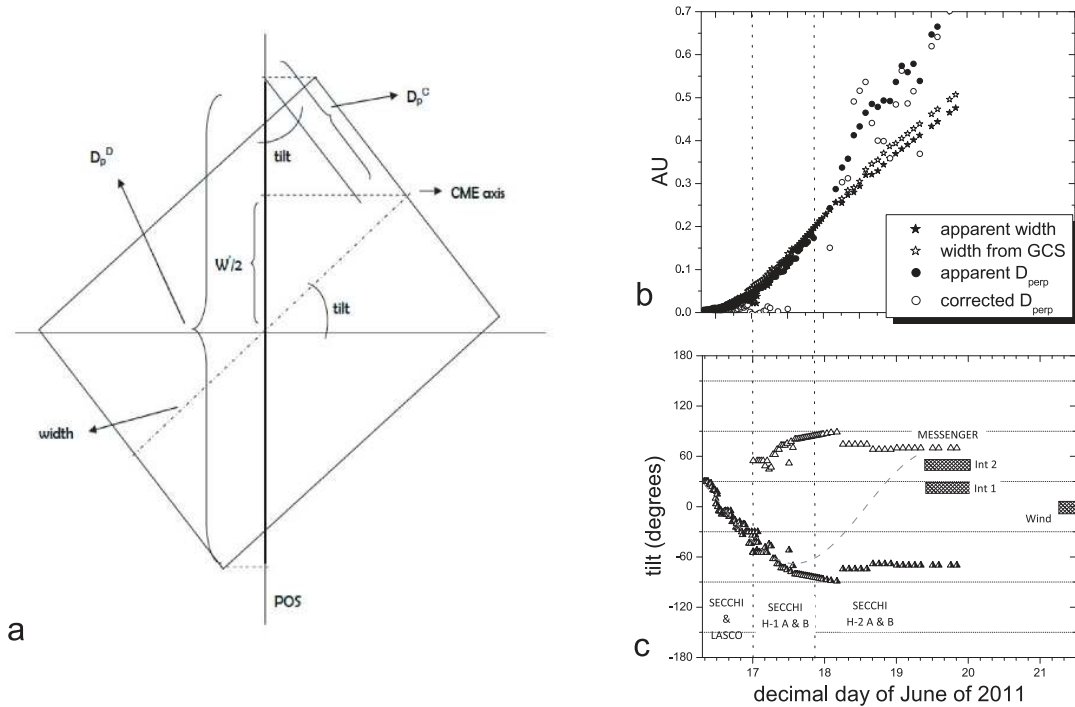


Figure 8. a) Correction, due to the CME/ICME rotation, to the projected perpendicular diameter measurements using the tilt and width (W) obtained from the GCS model. b) Shows perpendicular direct measurements of remote sensing data, the same data corrected due CME/ICME rotation and the width obtained by GCS technique and the projection onto the POS. c) The tilt of the CME from the low solar corona up to 1 AU. Filled triangles represent the values obtained with CSG technique. White triangles represent the symmetric tilt projection in the POS. The values obtained with the NFF in-situ model are shown by the two cross-hatched rectangles at 0.5 AU (two probable time intervals) and other at 1 AU. Vertical dash lines delimit the FOV detectors.

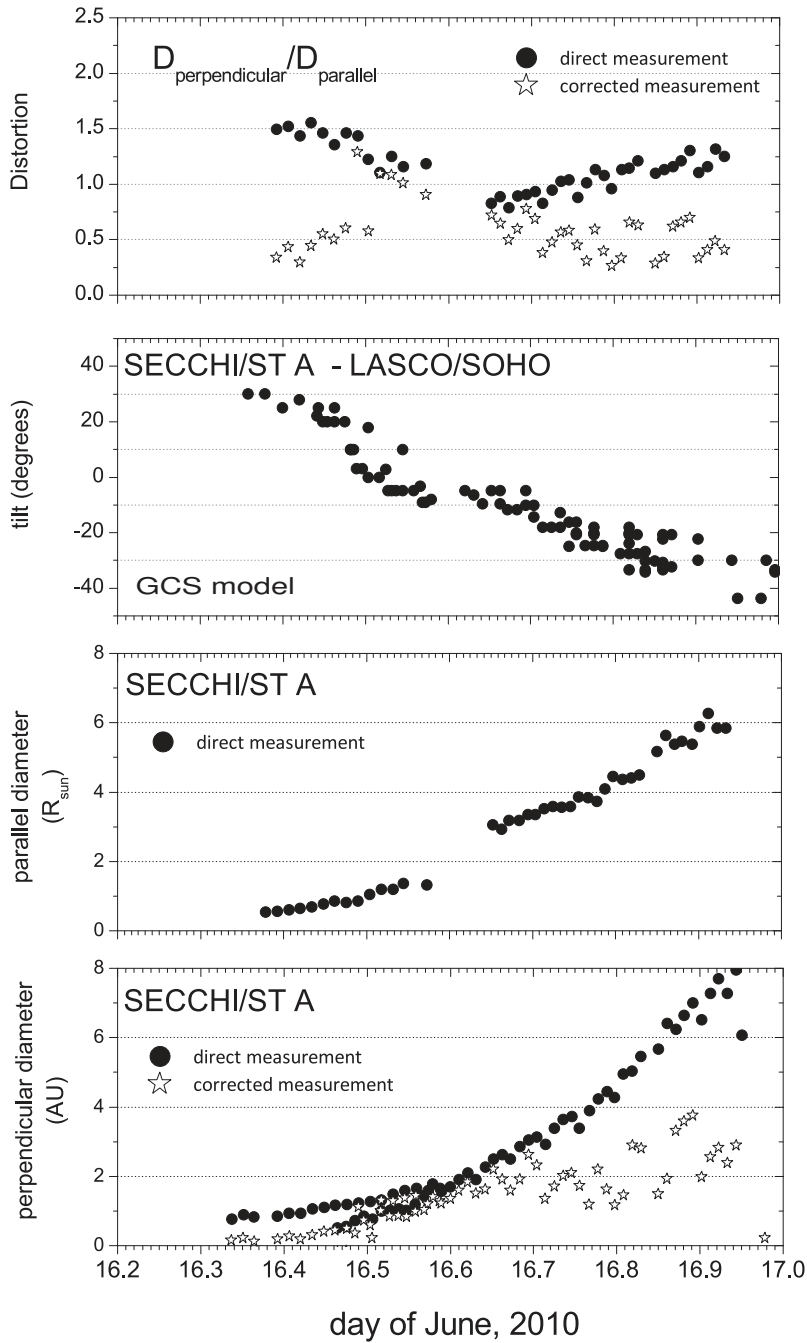


Figure 9. Combined analysis of the expansion and distortion of the CME/ICME for the period of time when LASCO/SOHO and SECCHI/STEREO spacecraft observed the event simultaneously. The best results from the GCS model are obtained when the CME is observed from all three viewpoints. From the bottom, the perpendicular direct (dots) and corrected measurement (stars), parallel diameter, tilt, and the distortion obtained from the direct and corrected data measurement are shown.

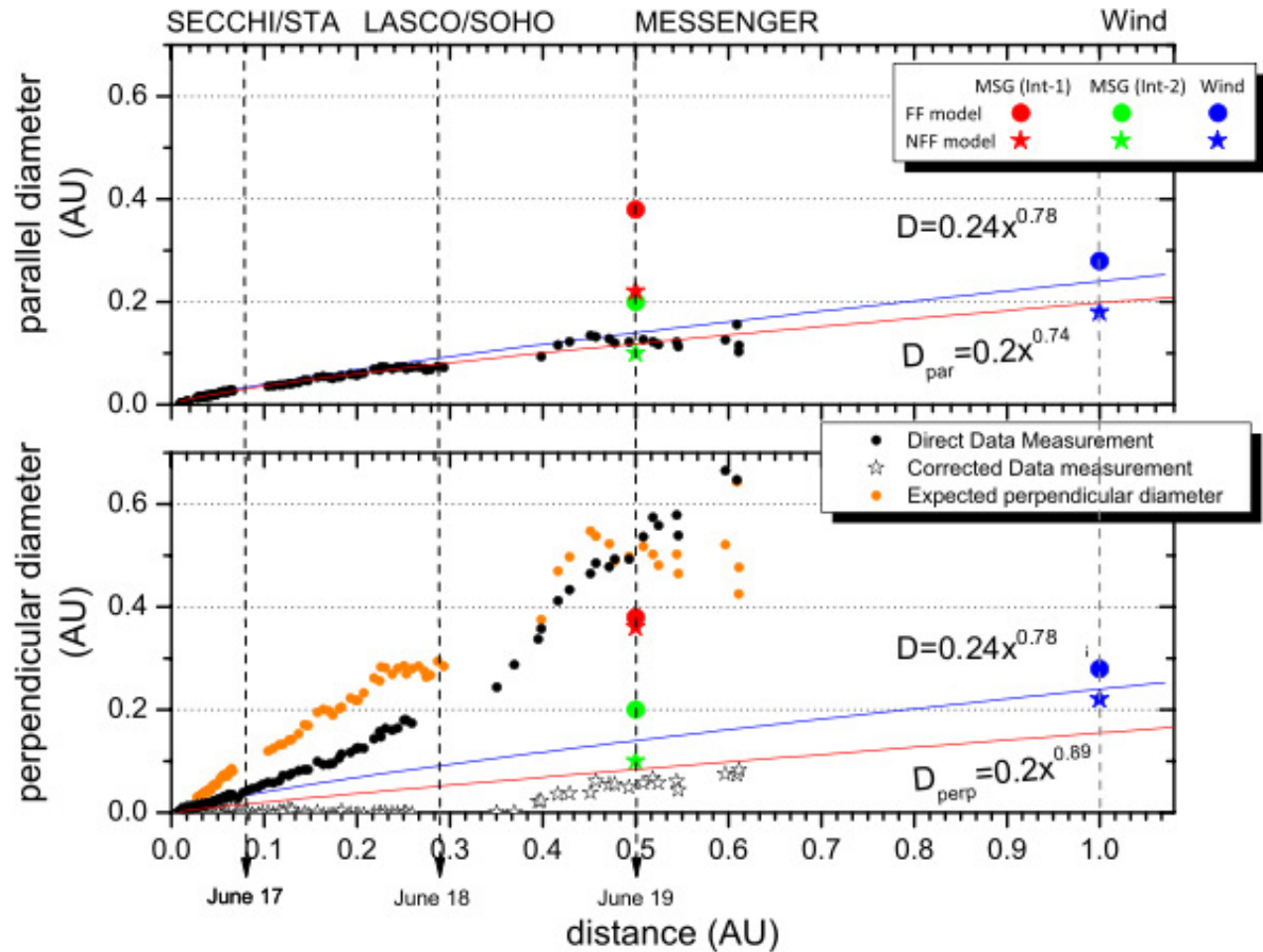


Figure 10. Combined analysis of the expansion of the parallel (top) and perpendicular (bottom) diameters of the ICME/CME cross section over 1 AU. The perpendicular diameters are corrected. Black dots represent the direct data measurements taken from the SECCHI/STEREO A images. Green and red dots/stars represent the results obtained with the in-situ analytical model at 0.5 and 1 AU. The blue lines are the empirically derived expansion assuming a circular cross section [Bothmer & Schwenn, 1998]. The red line represents the fit to the deprojected perpendicular data from Sun to 0.3 AU. Orange dots are the expected perpendicular diameters from Savani et al. [2011].

Table 1. The table on the top shows the observations by STEREO A and B: first time observation by each SECCHI detector (COR1, COR2, HI1 and HI2), the FOV (field of view) cover by detector, mean velocity and PA (pitch angle) measured in the interval. On the bottom table, from the in-situ observations of MESSENGER at 0.5 AU and Wind at 1 AU, the front and rear time for the MC boundaries, the mean velocity and the higher magnetic field detected by the magnetometer onboard each spacecraft.

REMOTE OBSERVATIONS

Spacecraft	FOV (R_{\odot})	T_{start} UT	V_{mean} (km/s)	PA ($^{\circ}$)
STEREO A/SECCHI				
COR1	1.4 - 4.0	Jun 16 06:05	64	96
COR2	2.5 - 15	Jun 16 11:08	206	88
HI1	15 - 86	Jun 16 22:06	389	87
HI2	68 - 318	Jun 18 02:09	299	89
STEREO B/SECCHI				
COR1	1.4 - 4.0	Jun 16 06:05	62	270
COR2	2.5 - 15	Jun 16 15:08	224	278
HI1	15 - 86	Jun 16 22:49	395	276
HI2	68 - 318	Jun 18 04:09	374	277
SOHO/LASCO				
C2	2.5 - 6.0	Jun 16 14:54	123	79
C3	4.0 - 30	Jun 16 19:42	294	62

IN-SITU OBSERVATIONS

Spacecraft	Position	T_{start}	T_{end}	V_{sw}	B_{max}	
MESSENGER	0.5 AU	Int-1 ^(**)	06/19/10 10:48:00	06/20/10 2:24:00	350 km/s ^(*)	31 nT
MESSENGER	0.5 AU	Int-2 ^(**)	06/19/10 3:45:00			
Wind	1 AU		06/21/10 7:12:00	06/22/10 7:12:00	365 km/s	8.6 nT

(*) V_{sw} is the estimated solar wind bulk velocity using the first time remote observation and the time arrival to Wind.

(**) Two possible start times for flux rope observed by MESSENGER.

Table 2. Parameters obtained with in-situ force-free (FF) circular model and non force-free (NFF) elliptical model. Two intervals have been chosen for MESSENGER data, table 1.

S/P	j_η $\mu\text{A}/\text{km}^2$	j_y^0 $\mu\text{A}/\text{km}^2$	B_y^0 nT	ϵ (%)	ϕ^{model} ($^\circ$)	$tilt^{model}$ ($^\circ$)	ξ ($^\circ$)	y_0 AU	R_{max} AU	ϕ_t 10^{20}Mx	j_0 $\mu\text{A}/\text{km}^2$	$corr$
MESS	Int-1											
NFF	0.45	0.35	43.86	55	120	38	158	0.067	0.180	60.2	0.5	0.52
FF			27.10		128	10		0.034	0.151	19.0	2.3	
MESS	Int-2											
NFF	1.92	3.66	29.00	96	144	43	159	0.017	0.049	4.7	8.02	0.64
FF			25.11		167	69		0.017	0.092	6.6	3.5	
Wind												
NFF	0.19	0.86	9.7	86	41	-14	174	0.046	0.104	6.8	0.68	0.86
FF			9.60		73	6		0.085	0.134	6.1	0.85	